A New Likelihood Function for Consistent Phase Series Estimation in Distributed Scatterer Interferometry

Chisheng Wang, Xiang-Sheng Wang, Yaping Xu, Bochen Zhang, *Member, IEEE*, Mi Jiang, *Senior Member, IEEE*, Siting Xiong, Qin Zhang, *Member, IEEE*, Weidong Li, and Qingquan Li

***Abstract*— The proper use of distributed scatterer (DS) can improve both the density and quality of synthetic aperture radar (SAR) interferometry (InSAR) measurements. A critical step in DS interferometry (DSI) is the restoration of a consistent phase series from SAR interferogram stacks. Most state-of-the-art algorithms adopt an approximate likelihood function to calculate the likelihood by replacing the true coherence matrix with its estimation, more specifically, the sample coherence matrix (SCM). However, this approximation has a drawback in that the coherence estimates are greatly biased when the coherence is low. In this study, we derive a new likelihood function without such an approximation. Accordingly, a DSI framework using this function for phase estimation and point selection is provided. In this framework, the new likelihood function serves as a cost function for phase estimation and a quality measure for DS selection. Its performance is investigated by experiments in a simulation study and a real-world case study using Sentinel-1 data over Shenzhen airport in China. The results reveal that the proposed DSI framework outperforms the existing state-of-the-art approaches in different scenarios, in terms of providing a more accurate estimation and improving DS density and coverage.**

***Index Terms*— Distributed scatterer (DS), interferometry, maximum likelihood, phase-linking (PL), synthetic aperture radar (SAR).**

Manuscript received January 24, 2022; revised April 5, 2022; accepted April 24, 2022. Date of publication April 26, 2022; date of current version May 10, 2022. This work was supported in part by the National Natural Science Foundation of China under Grant 41974006 and in part by the Shenzhen Scientific Research and the Development Funding Programmes under Grant RCYX20210706092140076 and Grant 20200812164904001. *(Corresponding author: Bochen Zhang.)*

Chisheng Wang is with the Ministry of Natural Resources (MNR) Key Laboratory for Geo-Environmental Monitoring of Great Bay Area, the Guangdong Key Laboratory of Urban Informatics, and the Shenzhen Key Laboratory of Spatial Smart Sensing and Services, School of Architecture and Urban Planning, Shenzhen University, Shenzhen 518060, China.

Xiang-Sheng Wang is with the Department of Mathematics, University of Louisiana at Lafayette, Lafayette, LA 70504 USA.

Yaping Xu is with the Department of Plant Sciences, The University of Tennessee, Knoxville, TN 37996 USA.

Bochen Zhang and Qingquan Li are with the College of Civil and Transportation Engineering, Shenzhen University, Shenzhen 518060, China (e-mail: bochen.zh@gmail.com).

Mi Jiang is with the School of Geospatial Engineering and Science, Sun Yat-sen University, Guangzhou 510275, China.

Siting Xiong is with the Guangdong Laboratory of Artificial Intelligence and Digital Economy (SZ), Shenzhen 518107, China.

Qin Zhang is with the College of Geology Engineering and Geomatics, Chang'an University, Xi'an 710061, China.

Weidong Li is with the School of Information Science and Engineering, Henan University of Technology, Zhengzhou 450001, China.

Digital Object Identifier 10.1109/TGRS.2022.3170567

I. Introduction

SYNTHETIC aperture radar (SAR) interferometry (InSAR) has been proven to be a powerful technique for deformation monitoring in the past decades [1], [2]. During the early stages, two or three repeat-pass InSAR processes using small image dataset were prevalent because large acquisitions were often not available. Early attempts to achieve accurate results were primarily focused on spatial filtering, and 2-D unwrapping algorithms and time-dependent noise could not be addressed because of the lack of time-series datasets in most areas. However, with the increasing number of SAR satellites launched in the 21st century, a large amount of SAR data have become available, and an increasing number of studies have turned to developing times-series analysis methods to exploit these large datasets (i.e., time-series images) for measuring more precise deformation [3]. These time-series methods can be primarily divided into two categories [4]: small baseline subsets (SBASs) [5]–[7] and permanent scatterers (PSs)-InSAR [8], [9]. They are still popular owing to their publicly accessible open-source code [10].

Although both the methods can deal with time-series SAR datasets, their theoretical fundamentals differ significantly from each other. More specifically, the radar backscatter of one pixel can be regarded as the summation of backscattering from all the scatterers within the image pixel. Based on the different scattering types, image pixels can be primarily classified as PS pixels and distributed scatterer (DS) pixels. In SBAS, PS and DS were normally not discriminatively processed; the interferometric phase on all the pixels was equally filtered using a multi-looking operator. A time-series analysis then is applied in a certain number of multi-looked interferograms with temporal and spatial baselines smaller than the given thresholds. Despite the great interest from researchers, the loss of spatial resolution and boxcar windows within SBAS limits its application at a finer scale. The contamination of neighboring pixels with different backscattering properties is likely to bias the optimal value to varying degrees, depending on scene complexity [11], and possibly bear a higher influence from the risk of bias [12]. PS-InSAR preserves the spatial resolutions for PS targets, on which the phase noise is mostly small. Therefore, PS-InSAR is more popular in urban environments, where PS pixels are abundant [13]. Regardless, the sparse distribution of permanent measurement points over natural

landscapes presents the primary challenge for unwrapping and atmospheric correction in InSAR time-series analyses [14].

The most recent advances in the InSAR community have focused on the integration of PS and DS to derive reliable and dense time-series deformation results [15], [16]. Among them, SqueeSAR refers to a representative work. SqueeSAR developed a DS interferometry (DSI) framework to integrate DS and PS in the time-series processing, including the statistical test for statistically homogeneous pixels (SHP) identification and phase triangulation algorithm (PTA) for consistent phase estimation [17]. Early efforts to optimize the DS phase have been documented in [18]–[20], where the authors attempted to estimate an accurate interferometric phase on DSs from interferogram stacks by exploring the target statistics and modeling the decorrelation characteristics. Following previous studies [19], we use the term phase-linking (PL) to refer to the estimation process of a consistent phase series from interferogram stacks. The steps in the joint DS–PS processing framework have been further refined by numerous works [21]–[23]. New algorithms have been developed to advance the speed and accuracy of identifying neighboring pixels [24], [25] and to optimize the selection of DS [26]. Robust estimation tools were implemented to ensure consistent quality of the coherence matrix under different statistical distributions [27].

Several advanced PL estimators have been proposed in recent years. For example, a sequential estimator was proposed to efficiently process a large number of SAR images [28]. Principal component analysis (PCA) was used in several studies to treat the multi-mechanism phenomenon in SAR signals [29], [30]. The eigen-decomposition-based maximum-likelihood estimator (MLE) of interferometric phase (EMI) was proposed to avoid the drawbacks of the PTA iterative method when estimating the non-positive coherence matrix [31]. Moreover, a bootstrapping method was proposed to balance the bias in covariance estimation for low-coherence points [22]. Notably, we used the coherence matrix rather than the covariance matrix in this study. This is a conventional approach to compensate for possible backscattered power imbalance by normalizing the amplitude values [29], [32].

From a mathematical point of view, these PL estimators differ mainly in the cost functions used to solve consistent phase series. Theoretically, MLE should be considered as the optimum choice because its root mean square error (RMSE) is asymptotically close to the expected lower boundary, that is, the Cramér–Rao lower bound (CRLB). Although most of these algorithms claim that they are MLEs, they use an approximate likelihood function, where the coherence matrix in the likelihood functions is approximated by the sample coherence matrix (SCM). As pointed out in many previous works [28], [33], the poor quality of the estimated coherence, which is common for low-coherent scatterers, would significantly contaminate the estimated consistent phase series. Accordingly, if a severely biased coherence matrix is used, PL resulting from full exploitation of interferograms would even be much more erroneous than some partial exploitation [21], [28]. Although recent studies have noticed this problem for low-coherent scatterers [33], [34], their attempts have primarily relied on developing distinct methods to calibrate the sampled coherence matrix, so that the approximate likelihood value can be close to the true value. These calibrations to the sampled coherence matrix can also be considered as regularization, which will be explained in more detail in Section III. Nevertheless, there is still a lack of research on deriving the mathematical form of the true likelihood function. Moreover, the benefits of using precise likelihood values for phase estimation have rarely been discussed.

In this study, we provide a mathematical formula to accurately represent the likelihood value of consistent phase series. Unlike the common approaches used in many PL methods, the proposed formula does not use SCM for approximation to calculate the likelihood value. A DSI framework using the new likelihood function for consistent phase series estimation and DS point selection is presented. Subsequently, we evaluated the performance of the proposed DSI approach by comparing it with the existing state-of-the-art approaches. The contributions of this study are as follows.

1) A precise function is provided to evaluate the likelihood of consistent phase series.
2) A multiple starting points' strategy is designed to optimize consistent phase series under the new likelihood function.
3) Several regularization schemes on SCM are designed to generate a series of PL solutions as starting points.
4) The advantage of the proposed likelihood function in selecting high-quality scatterers is examined.

The remainder of this article is organized as follows. Section II describes the mathematical work used to derive the new likelihood function. Section III presents the DSI framework with a new likelihood function. The experimental results are given in Section IV, and a real-world case study is presented in Section V. Finally, conclusions and perspectives are presented in Section VI.

II. Derivation of the New Likelihood Function

A. Role of Likelihood Function in DSI

Unlike PS pixels dominated by a stable scatterer with a very small phase variance, DS pixels do not have a dominant scatterer and the phase varies in a random manner. However, DS phase quality can be improved using a well-known PL process if the scatterers inside the DS pixel have similar scattering mechanisms. Here, SAR observation of one scatterer can be treated as a random complex variable. In accordance with the central limit theorem, the combination of a large number of independent scatterers tends toward a normal distribution. Therefore, SAR observation of a pixel with one scattering mechanism follows a circular complex Gaussian (CCG) distribution.

Given a statistical model, a likelihood function can be developed to describe the joint probability of the observed data as a function of unknown parameters. This function can be used to estimate unknowns and assess the quality of estimation. Therefore, when the statistical properties of a random variable are known, it is possible to make statistical inferences regarding the parameters of the variable based

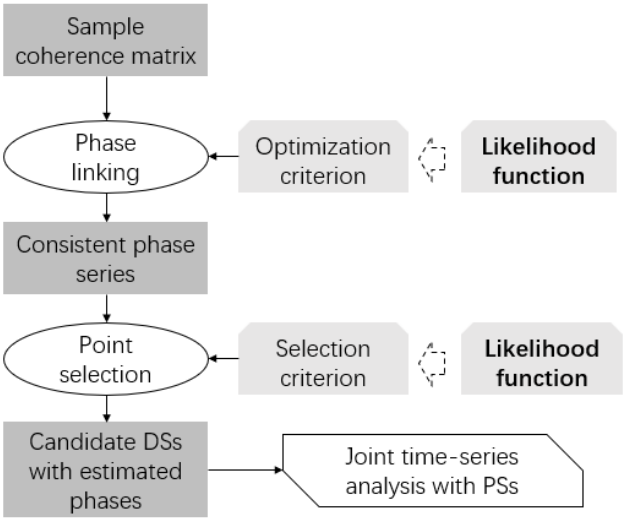

Fig. 1. General procedure for DSI.

on observations. PL is a process of statistical inference that attempts to estimate the time-series consistent interferometric phases of a DS pixel from its SAR observation samples.

There were three preliminary steps before PL. First, the SHP for each pixel was identified to prepare the samples. Second, pixels with an SHP number larger than a given threshold were selected. Third, we calculated the sample complex coherence matrix for these pixels using the identified SHPs. Subsequently, PL was implemented to calculate a consistent phase series from SCM. The potential DS pixels that exhibit high quality can then be treated as PS pixels. The original interferometric phases were replaced with the estimated consistent phase series. The traditional PS time-series processing algorithms can then be adopted to jointly process DS and PS pixels. These steps form the standard DSI procedure, as shown in Fig. 1.

Both PL and point selection in DSI require a quantitative function to assess the quality of a consistent phase series solution. The likelihood function describes the joint probability of the observed data as a function of unknown parameters of the chosen statistical model. It can naturally serve as a quantitative criterion for PL and point selection. In Fig. 1, we used a dashed arrow to connect the likelihood function with the optimization criterion and selection criterion. This is because the functions used by many DSI algorithms are not the exact form of the likelihood function under the CGG statistical model, as described below. However, these functions also represent the acceptability or probability of a solution given the SAR observations. They share similar forms or characters with a true likelihood function.

B. Mathematical Background of the Likelihood Function

According to CGG assumption, the probability density function (PDF) of the time-series data vector $\mathbf{z}$ of a pixel conditioned on the coherence matrix is as follows:

$$f(\mathbf{z}) = \pi^{-p}\left(\det[\boldsymbol{G}]\right)^{-1}\exp\left(-\mathbf{z}^{\mathrm{H}}\boldsymbol{\Theta}\mathbf{G}^{-1}\boldsymbol{\Theta}^{\mathrm{H}}\mathbf{z}\right) \tag{1}$$

where

$p \in \mathbb{N}$:	number of single look complex (SLC) images;
$\mathbf{z} \in \mathbb{C}^{p\times 1}$:	random SLC observation vector along time for a pixel;
$\boldsymbol{G} \in \mathbb{R}^{p\times p}$:	real-value coherence matrix of the interferograms for a pixel;
$\boldsymbol{\theta} \in \mathbb{R}^{p\times 1}$:	consistent phase series for a pixel;
$\boldsymbol{\Theta} \in \mathbb{C}^{p\times p}$:	complex matrix containing consistent phase series $\boldsymbol{\theta}$ with $\boldsymbol{\Theta} = \mathrm{diag}[\mathrm{e}^{\mathrm{i}\boldsymbol{\theta}}]$;
det :	determinant operator.

Under the one scattering mechanism assumption, the complex coherence matrix $\boldsymbol{\Gamma} \in \mathbb{C}^{p\times p}$ can be given as follows:

$$\boldsymbol{\Gamma} = \boldsymbol{\Theta}\boldsymbol{G}\boldsymbol{\Theta}^{\mathrm{H}}. \tag{2}$$

If $\boldsymbol{G}$ is known, the maximum likelihood estimation of phase is given by

$$\hat{\boldsymbol{\theta}} = \arg\max\left\{(\mathrm{e}^{\mathrm{i}\boldsymbol{\theta}})^{\mathrm{H}}\left(-\boldsymbol{G}^{-1}\circ\hat{\boldsymbol{\Gamma}}\right)\mathrm{e}^{\mathrm{i}\boldsymbol{\theta}}\right\} \tag{3}$$

where $\hat{\boldsymbol{\Gamma}}$ denotes the SCM, given by

$$\hat{\boldsymbol{\Gamma}} = E\left[\mathbf{z}\mathbf{z}^{H}\right] \approx \frac{\mathbf{1}}{N}\sum_{\mathbf{z}\in\Omega}\mathbf{z}\mathbf{z}^{H} \tag{4}$$

where $\boldsymbol{\Omega}$ denotes a homogeneous patch containing adjacent pixels, N signifies the number of adjacent pixels in the homogeneous patch, and E indicates the expectation operator.

Since the true real-value coherence matrix $\boldsymbol{G}$ is unknown, generally the absolute values of the sample complex coherence matrix $\left|\hat{\boldsymbol{\Gamma}}\right|$ are considered for replacement [17]. Equation (3) can then be written as follows:

$$\hat{\boldsymbol{\theta}} = \arg\max\left\{(\mathrm{e}^{\mathrm{i}\boldsymbol{\theta}})^{H}\left(-\left|\hat{\boldsymbol{\Gamma}}\right|^{-\mathbf{1}}\circ\hat{\boldsymbol{\Gamma}}\right)\mathrm{e}^{\mathrm{i}\boldsymbol{\theta}}\right\}. \tag{5}$$

The problem is that a poor estimation of SCM contaminates the PL results. In addition, if SCM is not positive definite, additional work on SCM is required, such as inserting a damping factor [27] or including calibration parameters [31].

C. New Likelihood Function

Theoretically, the solution of an MLE should have maximum probability. However, as described above, the MLE approach in existing studies often uses an SCM to replace the true coherence matrix and provide estimated MLE solutions that are only approximate. In this section, a mathematical formula is derived to represent the true likelihood and achieve true maximum likelihood estimation (TMLE).

We take the natural logarithm of PDF in (1) and obtain

$$L(\boldsymbol{\theta}, \boldsymbol{G}) = -Np\ln(\pi) - N\ln[\det(\boldsymbol{G})] - \sum_{k=1}^{N}\mathbf{z}_k^{H}\boldsymbol{\Theta}\boldsymbol{G}^{-1}\boldsymbol{\Theta}^{H}\mathbf{z}_k \tag{6}$$

where ln symbolizes the natural logarithm operator.

Here, the SAR complex data $\mathbf{z}$ are given as observation, and the consistent phase series $\boldsymbol{\theta}$ and real-value coherence matrix $\boldsymbol{G}$ are treated as unknown parameters. It differs from the state-of-the-art PL algorithms that only consider $\boldsymbol{\theta}$ as unknowns and use a sample covariance matrix to approximate $\boldsymbol{G}$.

Since the logarithm is a monotonic function, the maximum of $L(\boldsymbol{\theta}, \boldsymbol{G})$ occurs at the same values of $\boldsymbol{\theta}$ and $\boldsymbol{G}$ as does the maximum of PDF. The MLE of $\boldsymbol{\theta}$ and $\boldsymbol{G}$ can be achieved by maximizing the $L(\boldsymbol{\theta}, \boldsymbol{G})$ function. Accordingly, the necessary conditions for a maximum are

$$0 = \frac{\partial L}{\partial \boldsymbol{G}}, 0 = \frac{\partial L}{\partial \boldsymbol{\theta}}. \tag{7}$$

Here, we introduce a new matrix parameter $\boldsymbol{R}$, defined as the inverse of $\boldsymbol{G}$

$$\boldsymbol{R} = \boldsymbol{G}^{-1}. \tag{8}$$

For convenience, we define

$$\boldsymbol{Q} = \frac{1}{N}\mathrm{Re}\left(\sum_{k=1}^{N} \boldsymbol{\Theta}^H \mathbf{z}_k \mathbf{z}_k^H \boldsymbol{\Theta}\right) \tag{9}$$

where Re denotes the real part operator of complex values.

Equation (6) can be transferred to a simple form

$$L(\boldsymbol{\theta}, \boldsymbol{R}) = -Np\ln(\pi) + N\left[\ln(\det[\boldsymbol{R}]) - \mathrm{tr}(\boldsymbol{R}\boldsymbol{Q})\right] \tag{10}$$

where tr denotes the trace operator.

To satisfy the maximum condition, we made a partial derivative of $L(\boldsymbol{\theta}, \boldsymbol{R})$ and obtain

$$0 = \frac{\partial L}{\partial \boldsymbol{R}} = N\left(\boldsymbol{R}^{-1} - \boldsymbol{Q}\right). \tag{11}$$

Therefore, the MLE of $\boldsymbol{G}$ or $\boldsymbol{R}$ is derived

$$\boldsymbol{G} = \boldsymbol{R}^{-1} = \boldsymbol{Q} = \frac{1}{N}\mathrm{Re}\left(\sum_{k=1}^{N} \boldsymbol{\Theta}^H \mathbf{z}_k \mathbf{z}_k^H \boldsymbol{\Theta}\right) = \mathrm{Re}\boldsymbol{\Theta}^H \hat{\boldsymbol{\Gamma}} \boldsymbol{\Theta}. \tag{12}$$

For abbreviation, we introduced matrix variable $\boldsymbol{W}$

$$\boldsymbol{W} = \boldsymbol{\Theta}^H \hat{\boldsymbol{\Gamma}} \boldsymbol{\Theta}.$$

Since $\boldsymbol{R}\boldsymbol{Q} = \boldsymbol{I}$ and $\boldsymbol{G} = \boldsymbol{R}^{-1} = \mathrm{Re}(\boldsymbol{W})$, the function $L(\boldsymbol{\theta}, \boldsymbol{R})$ can be rewritten as follows:

$$L(\boldsymbol{\theta}) = -Np\ln(\pi) - N\ln[\det(\mathrm{Re}[\boldsymbol{W}])] - Np.$$

Here, the parameter $\boldsymbol{G}$ or $\boldsymbol{R}$ is eliminated from the function and only parameter $\boldsymbol{\theta}$ is left. Therefore, the maximum likelihood estimation of phase $\boldsymbol{\theta}$ is given by

$$\begin{aligned}\hat{\theta} &= \arg\max\{-Np\ln(\pi) - N\ln[\det(\mathrm{Re}[\boldsymbol{W}])] - Np\} \\ &= \arg\max\{-\det(\mathrm{Re}[\boldsymbol{W}])\}.\end{aligned} \tag{13}$$

A significant difference between (5) and (13) is that we use a maximum likelihood estimation of $\boldsymbol{G}$ rather than an approximated one (i.e., $|\hat{\boldsymbol{\Gamma}}|$). Thus, the likelihood function strictly adheres to the statistical model and can truly represent the likelihood value of a given solution. This is unaffected by the poor estimation of SCM.

In summary, we successfully derived the mathematical form of the new likelihood function, $-\det(\mathrm{Re}[\boldsymbol{W}])$, which strictly adheres to the assumed statistical model without any approximation. We used the term $-$detR to represent the calculated new likelihood value. Notably, detR and lg(detR) are also used to represent the negative and common logarithmic forms of the likelihood value, respectively. In Section II, we demonstrate how this function is used in phase estimation and DS point selection for DSI.

TABLE I

SUMMARY OF THE COMPARISON AMONG THE FOUR PL ALGORITHMS

Methods	Coherence model, $\boldsymbol{\Gamma}$	Optimization/Likelihood functions
TMLE	$\boldsymbol{\Theta}\boldsymbol{G}\boldsymbol{\Theta}^{\mathrm{H}}$	$\arg\max\{-\det(\mathrm{Re}[\boldsymbol{\Theta}^H\hat{\boldsymbol{\Gamma}}\boldsymbol{\Theta}])\}$
PTA	$\boldsymbol{\Theta}\lvert\hat{\boldsymbol{\Gamma}}\rvert\boldsymbol{\Theta}^{\mathrm{H}}$	$\arg\max\left\{(\mathrm{e}^{\mathrm{i}\boldsymbol{\theta}})^{\mathrm{H}}\left(-\lvert\hat{\boldsymbol{\Gamma}}\rvert^{-1}\circ\hat{\boldsymbol{\Gamma}}\right)\mathrm{e}^{\mathrm{i}\boldsymbol{\theta}}\right\}$
PCA	$\sum_{i=1}^{p}\boldsymbol{\Theta}_i\boldsymbol{G}_i\boldsymbol{\Theta}_i^{\mathrm{H}}$	$\arg\max\{(\lvert\boldsymbol{v_1}\rvert\circ\mathrm{e}^{\mathrm{i}\boldsymbol{\theta}})^{\mathrm{H}}(\hat{\boldsymbol{\Gamma}})(\lvert\boldsymbol{v_1}\rvert\circ\mathrm{e}^{\mathrm{i}\boldsymbol{\theta}})\}$
EMI	$\boldsymbol{\sigma}\boldsymbol{\sigma}^T\circ\boldsymbol{\Theta}\lvert\hat{\boldsymbol{\Gamma}}\rvert\boldsymbol{\Theta}^{\mathrm{H}}$	$\arg\max\left\{(\boldsymbol{\sigma}\circ\mathrm{e}^{\mathrm{i}\boldsymbol{\theta}})^{\mathrm{H}}\left(-\lvert\hat{\boldsymbol{\Gamma}}\rvert^{-1}\circ\hat{\boldsymbol{\Gamma}}\right)(\boldsymbol{\sigma}\circ\mathrm{e}^{\mathrm{i}\boldsymbol{\theta}})\right\}$

III. NEW LIKELIHOOD FUNCTION FOR DSI

A. New Likelihood Function for PL

The principal role of the proposed likelihood function is PL. Accordingly, we can obtain an optimal consistent phase series by searching for its maxima. The new likelihood function (13) is a determinant of the p-dimensional matrix (p = SLC image number), which is a polynomial of degree p. However, the likelihood functions of the PL algorithms listed in Table I are only polynomials with a degree of two. The primary challenges brought by the high-degree function were the high time cost for optimization and the risk of falling into local maxima. To increase the search speed, we used the solution from other PL methods as the starting point for skipping less meaningless searching. Moreover, we adopted a multiple starting point strategy to avoid falling into local minima. We used solutions from other PL methods as the potential starting points. Subsequently, we evaluated them using their likelihood values and then selected the best solution for the final optimization. Since the true likelihood value was used, we named this PL approach the TMLE.

Naturally, we can resort to the existing efficient PL algorithms to generate initial guess solutions. Here, we first demonstrate that many state-of-the-art PL algorithms can be treated as estimators using regularized SCM (RSCM). The differences between them were due to the regularization forms. By unifying these PL algorithms in terms of regularization, we can infer a new series of estimators using different regularization parameters. The number of candidate solutions can correspondingly increase and benefit solution optimization.

In most state-of-the-art PL algorithms, SCM is used as a replacement for the true covariance matrix. If so, the positive definite condition of SCM should be satisfied. Otherwise, (3) cannot be calculated because the inverse of SCM does not exist. To satisfy the positive definite requirement, regularization is required when the smallest eigenvalues of the SCM are numerically close to zero. A singular SCM is commonly observed in two cases: 1) a small sample size and 2) high coherence. A fundamental requirement for positive definite SCM is to have sufficient uncorrelated samples. Undoubtedly, samples smaller than the SLC image number will create a rank-deficient SCM. Meanwhile, if the samples are highly correlated, the SCM will also be non-positive definite even when the size is sufficiently large (see Fig. 2). This is because the highly coherent pixels are less affected by noise and often have very similar temporal characteristics as their neighboring homogeneous pixels. Therefore, the SHPs for a

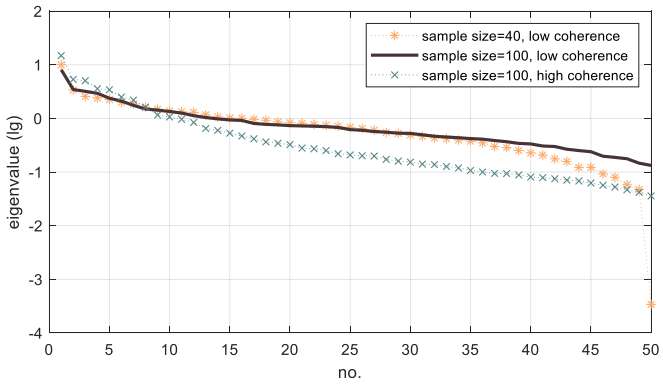

Fig. 2. Eigenvalues of SCMs in two scenarios (dash lines) requiring regularization. The solid black line is considered a reference, denoting the case that does not require regularization.

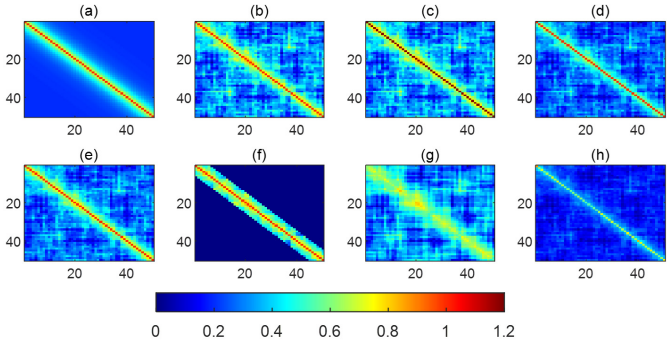

Fig. 3. Matrix after different regularization approaches. (a) Input coherence model. (b) SCM. (c) RSCM by Reg 1. (d) RSCM by Reg 2. (e) RSCM by Reg 3. (f) RSCM by Reg 4. (g) RSCM by Reg 5. (h) RSCM by Reg 6.

highly coherent pixel are often highly correlated and create an ill-posed or rank-deficient SCM.

Regularization is an efficient approach to deal with unstable estimations [35] and is widely applied to handle ill-posed problems. The general idea of SCM regularization is to blend a poor matrix estimate with a stable known matrix. Given an SCM $\hat{\Gamma}$, it can be regularized by forming an estimate

$$\hat{\mathbf{\Gamma}}_r = \alpha\hat{\mathbf{\Gamma}} + \beta\boldsymbol{K} \tag{14}$$

where α and β denote the regularization factors, $\boldsymbol{K}$ indicates the stable known matrix, and $\hat{\mathbf{\Gamma}}_r$ refers to the RSCM. Several regularization methods are listed below, and many state-of-the-art PL algorithms can be described in this regularization form (see Fig. 3).

1) Regularization by gradually inserting a damping factor (Reg 1) is a commonly used regularization method in the PTA algorithm to treat rank-deficient SCM. It sets $\alpha = 1$ and $\boldsymbol{K} = \mathbf{I}$, and lets β gradually increase until $\hat{\mathbf{\Gamma}}_r$ is positive definite.
2) Regularization using an identity matrix (Reg 2) sets $\beta = 1-\alpha$ and $\boldsymbol{K} = \mathbf{I}$. α is considered a regularization factor ranging from 0 to 1.
3) Regularization using pooled SCM (Reg 3) sets $\beta = 1-\alpha$ and $\boldsymbol{K} = \hat{\mathbf{\Gamma}}_p$, where $\hat{\mathbf{\Gamma}}_p$ denotes the pooled estimate of SCM. The idea behind the pooled estimate is to pool samples from other classes to increase the sample size. In our case, we can enlarge the search box to include more SHPs in the pooled SCM estimation.
4) Regularization by masking long-term coherence (Reg 4) sets $\alpha = \beta = 1$ and $\boldsymbol{K} = -\hat{\mathbf{\Gamma}}_d$, where $\hat{\mathbf{\Gamma}}_d$ symbolizes a partial SCM with short-term elements (spanning days $< d$) masked. Then, the long-term coherence in RSCM becomes zero. Therefore, this regularization method can approach PL using a short temporal baseline subset (StBAS) [28].
5) Regularization by singular value decomposition (SVD) (Reg 5) is applied to SCM and only retains the component associated with the largest eigenvalues. When only the largest component is maintained, the new RSCM naturally has a consistent interferometric phase, and the consistent phase series can then be retrieved directly from any row of the RSCM without optimization. We note that this regularization method is the same as that of the PCA PL method.
6) Regularization using calibration parameters (Reg 6) sets $\alpha = \beta = 1$ and $\boldsymbol{K} = (\boldsymbol{\sigma}\boldsymbol{\sigma}^{\boldsymbol{T}} - \boldsymbol{I}) \circ \hat{\mathbf{\Gamma}}$, where $\boldsymbol{\sigma}$ denotes the calibration vectors. Both EMI and bootstrapping SCM bias corrections can be described in this form. The difference between them lies in the determination of the calibration parameters.

In the present study, we adopted the above regularization methods to generate a series of RSCMs (different regularization parameters are used), and then adopted the PTA to generate the candidate PL solutions. The detR function is taken to select the best initial guess and guide the final optimal solution searching. It should be mentioned that the state-of-the-art PL algorithms including PTA, PCA, and EMI are all contained in this regularization framework, which corresponds to regularization 1, 5, and 6, respectively

Furthermore, we want to point out that although we adopted regularization during phase solving, our final optimal solution should not be considered a regularized solution. This is because regularization is implemented on SCM and not on phase solution. Our likelihood function represents the true likelihood, without including any regularization components. Accordingly, the purpose of applying regularization to SCM is to derive approximate MLE solutions and help locate globally optimal solutions more easily. The TMLE solution inherits the main statistical characteristics of MLE, that is, it is asymptotically unbiased, asymptotically efficient, and consistent. Conversely, a regularized estimator inevitably generates a biased solution.

B. Comparison With Other PL Algorithms

We compared the TMLE with several prevalent estimators, that is, PTA, EMI, and PCA, primarily in terms of the assumptions used in the models and their computational efficiency. The investigated complex coherence matrix models and their optimization functions are listed in Table I.

1) Model assumption: TMLE, PTA, and EMI assume a single scatterer mechanism, whereas PCA assumes multiple mechanisms. Among the single-mechanism approaches, TMLE is the only method that strictly follows a

single-mechanism assumption without any additional assumptions. Meanwhile, the PTA method assumes that the real-value coherence matrix is equal to SCM. The EMI method also assumes a real-value coherence matrix, but in a different form: some calibration parameters were added to SCM to define the real-value coherence matrix. For multiple mechanisms, PCA assumes a covariance model combined with p (i.e., SLC number) orthogonal scattering mechanisms.

2) Computational efficiency: EMI and PCA are based on eigen decomposition, whereas PTA and TMLE rely on iterative optimizations. Although eigen decomposition is embedded with an iteration to obtain eigenpairs, the availability of optimized numerical recipes promises a highly efficient solution. In their existing forms, PTA and TMLE require more computational cost than PCA and EMI, and TMLE is more time-consuming than PTA. However, the computational efficiency is expected to improve if additional effort is put into the optimization algorithm. In addition, the iteration number for TMLE can be reduced to zero to save computational time. A zero iteration means that the detR function is only considered as a criterion to select the best solution from the candidates.

C. New Likelihood Function for Point Selection

In addition to its main role in PL, the new likelihood function can be used as a quality measure for DS point selection. Posterior coherence is the most commonly used point selection criterion in PL methods. The form of posterior coherence (γ) is given as [31], [32]

$$\gamma = \frac{2}{p^2 - p}\mathrm{Re}\left(\sum_{i=1}^{p}\sum_{k=i+1}^{p}\exp(\mathrm{i}\phi_{ik})\exp(-i[\theta_i - \theta_k])\right) \quad (15)$$

where ϕ_{ik} denotes the interferometric phase contained in the sampled coherence matrix, $\hat{\mathbf{\Gamma}}$.

As shown by the formula, the posterior coherence represents the equal-weighted phase fitness. It is also the cost function used by the equal-weighted PTA [36]. However, a higher posterior coherence does not necessarily indicate a less erroneous solution, because if it does, the equal-weighted PTA would be the optimum estimator, which, however, is not the case [36].

Therefore, we propose using the likelihood value calculated by the new function as the DS point selection criteria. As detR directly reveals the likelihood of a solution, it has the potential to act as an index for DS selection. Different types of scatterers are expected to be more distinguishable in detR map than posterior coherence. Since the detR value varies in a large range, we would use the common logarithm of detR below, i.e., lg(detR), for better plotting.

D. Algorithm Summary

We provide a brief summary of the new DSI framework using the proposed likelihood function (see Fig. 4). It follows these steps.

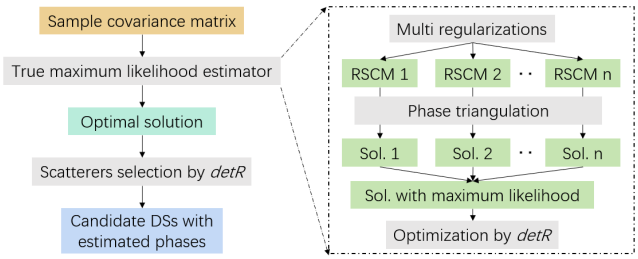

Fig. 4. Diagram of DSI using the proposed likelihood function.

TABLE II
TESTED ALGORITHMS AND DECORRELATION MODELS

Methods	Decorrelation models
TMLE	**Short-term (Coh 1)**
	γ_0=0.6, γ_∞=0, γ_p=0, τ_0=50d
PTA	**Periodic (Coh 2)**
PCA	γ_0=0.6, γ_∞=0, γ_p=0.2, τ_0=50d
EMI	**Long-term (Coh 3)**
	γ_0=0.6, γ_∞=0.2, γ_p=0, τ_0=50 d

1) The SCM of pixels with SHP number larger than a given threshold is calculated from the time-series images.
2) Multi-regularizations are applied to SCM with different regularization approaches and regularization factors.
3) Phase triangulation is implemented on these RSCMs to obtain a series of solutions.
4) An optimization is performed to maximize the likelihood value represented by −detR, using the best solution obtained from the third step as the starting point. The outputs in this step include the estimated consistent phase series and the corresponding likelihood value.
5) The candidate DS points are selected based on the detR values, and these selected DSs are then integrated with PSs for joint time-series analysis.

IV. SIMULATION

A. Experiment Setting

In the simulation, we used a modified exponential temporal decorrelation model according to a previous study [31] that can represent short-term, periodic, and long-term coherence. The decorrelation model for a single-mechanism DS is given by the following expression:

$$\boldsymbol{G}_{i,j} = (\gamma_0 - \gamma_\mathrm{p} - \gamma_\infty)\exp\left(\frac{-t_{i,j}}{\tau_0}\right) + \gamma_\mathrm{p}\exp\left(\frac{-\mathrm{mod}(t_{i,j}, t_\mathrm{p})}{\tau_0}\right) + \gamma_\infty \quad (16)$$

where $\boldsymbol{G}_{i,j}$ represents the real-value coherence between the ith and jth SLC. γ_0, γ_p, and γ_∞ denote the initial coherence, periodic coherence, and long-term coherence, respectively. mod is the modulo operation. $t_{i,j}$ indicates the time between the two SLCs. t_p refers to the return period for the periodic coherence. τ_0 denotes a constant that represents the decorrelation speed.

We used a normalized amplitude ($|\mathbf{z}_i| = 1$), such that the coherence was the same as the covariance. The CCG process was assumed in SLC complex data simulation. The stationarity and ergodicity assumptions were completely held;

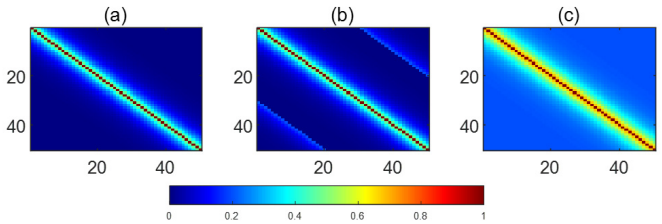

Fig. 5. Coherence matrices for three decorrelation models. (a) Short-term. (b) Periodic. (c) Long-term.

therefore, homogeneous samples were generated with the same distribution. The temporal sampling interval was set to 12 days, according to Sentinel-1 SAR data. Moreover, the initial coherence γ_0 was set as 0.6 according to previous studies [31], [33]. Examples of the short coherence, long coherence, and periodic coherence decorrelation models are illustrated in Fig. 5. Three state-of-the-art PL algorithms (PTA, PCA, and EMI) were compared with the proposed TMLE method (see Table II). Furthermore, CRLB was used as a reference. Their performances were quantitatively assessed by RMSE, which was calculated using the estimation results from 1000 realizations. In the simulation, the period cover was set to 600 days, which was equal to 50 SAR image acquisitions. The sample size was set at 300. In addition to containing the deformation signal, the phase to be solved also contains atmospheric and orbital signals, which are often distributed randomly temporally. Therefore, the true consistent phase series was randomly initiated, without assuming any temporal pattern.

B. Performance in PL

First, we investigated the influence of using detR for phase estimation by examining the performance of TMLE (see Fig. 6). Obviously, the proposed method outperforms other methods significantly in the short-term (Coh 1) and periodic decorrelation (Coh 2) models. In these two scenarios, RMSEs are smaller than the others. TMLE has maximum RMSEs of 0.63 and 0.24 rad for the short-term model and the periodic decorrelation models, respectively. Meanwhile, other PL methods give maximum RMSEs of 1.27–1.48 and 0.32–0.52 rad. For very bad conditions (i.e., low coherence), such as the phase estimation of the last SLC in the short-term model, the TMLE results approach the real value much better than PTA, with a reduction of approximately 1 rad RMSE. For the long-term decorrelation model (Coh 3), the differences between PL algorithms are not very significant. The maximum RMSEs are very small (approximately 0.11 rad), which is very close to the maximum value of CRLB (0.10 rad). It makes sense because the challenge in good coherence conditions is small, and the improvement from using more advanced algorithms is not very significant. The PCA method underperforms the other methods among all the decorrelation models. It is reasonable as the assumption (multi scattering mechanisms) held in PCA deviates from our simulation data setting (single scattering mechanism).

C. Role of Initial Guess Solutions in TMLE

In Section III-A, we denote the new likelihood function as a polynomial with a much higher degree than previous likelihood functions. Therefore, it is not possible to directly search for the global maxima. Using an initial guess is a practical method to determine the maxima in TMLE. The choice of initial solutions and the searching time are two crucial factors that affect TMLE performance. In this section, we explore these factors.

First, we displayed the distribution of the selected starting point to determine where the optimal solution originated. In our experiment, the candidate starting points were from five regularization methods, that is, Reg 1 and 2, and Reg 4–6. Reg 3 was not used in the simulation because the pooled samples could not be simulated fairly; however, it was adopted in the real case. As mentioned above, the PTA, PCA, and EMI methods can be grouped as Reg 1, Reg 5, and Reg 6, respectively. Therefore, we used them to represent these regularization methods. For Reg 2, the regularization factor (α) was varied from 0.1 to 1, and nine candidate solutions were created. For regularization 3, we set the regularization factor (d, i.e., mask bandwidth) from 1 to 49 and obtained 49 candidate solutions. From the distribution of the selected starting point, we found that solution selection is highly related to the coherence model. The detR function prefers to take the solution from Reg 2 and Reg 4 for relatively low coherent models (Coh1 and Coh2) and EMI for long-term model (see Fig. 7).

It has been revealed that PL using an StBAS exhibits better performance for the short-term coherence model compared with using all interferograms [28]. In low-coherence scenarios, long-term coherence is severely misestimated and further affects the accuracy of phase estimation. StBAS ignores interferograms with long temporal baselines and is therefore immune to this type of coherence error. As denoted in Section III, StBAS is equal to the fourth regularization (i.e., Reg 4). Similar to StBAS, Reg 2 adopts an identity matrix to regularize SCM and can also reduce the influence of off-diagonal elements. As illustrated in Fig. 6, TMLE can adaptively pick starting points from Reg 2 and Reg 4 for relatively low coherent models (Coh1 and Coh2), promising high performance in these cases. Although Reg 2 and Reg 4 perform well in the low-coherence case, they incur the cost of losing long-term interferograms and fail in the long-term coherence model. For Coh 3, it was found that TMLE takes starting points from EMI and Reg 4 with slight regularization (large d) and successfully avoided such problem that could be found in Reg 2 and Reg 4. It validates that the detR function can correctly provide a quantitative likelihood for each solution, and the proposed estimator (TMLE) can adaptively select the most suitable start solutions, ensuring high performance in all the coherence models.

To determine how the search time affects the TMLE performance, we limited the initial guess to only PTA solution and gradually increased the number of iterations. Five maximum iteration numbers were tested (100, 800, 2000, 3000, and 5000). We labeled them PTA1, PTA2, PTA3, PTA4, and PTA5, respectively. The time cost was calculated based on 1000 realizations. The results show that the optimization step can significantly reduce RMSE compared with the original PTA solution. The more the searching efforts, the less RMSE can be achieved. However, when the number of iterations reached

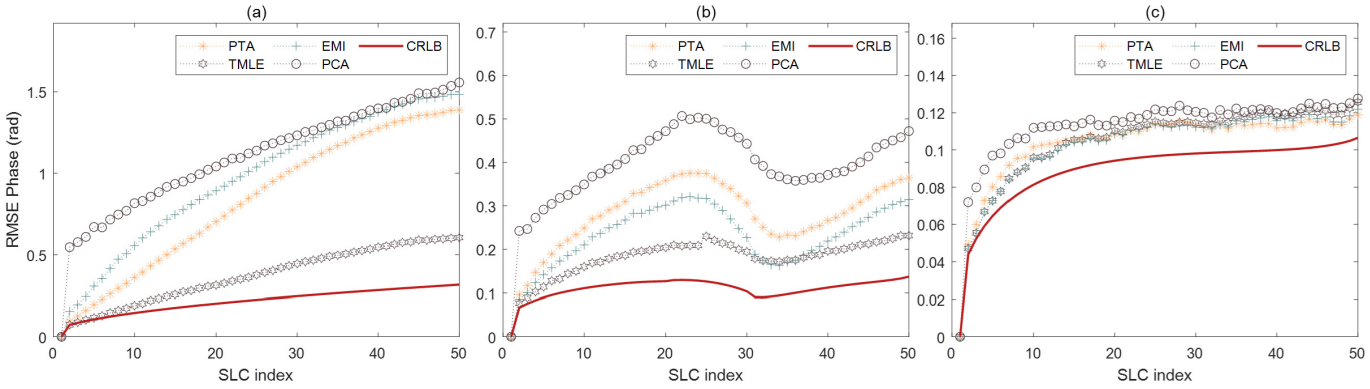

Fig. 6. RMSE of the compared PL algorithms. (a) Short-term. (b) Periodic. (c) Long-term.

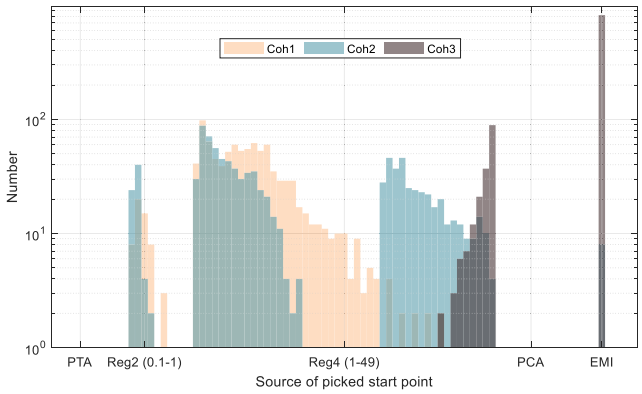

Fig. 7. Histogram of initial guess solutions (regularization approaches) selected by the detR function.

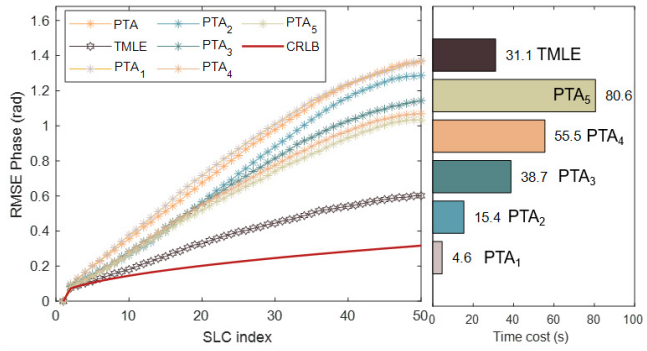

Fig. 8. TMLE results with different iteration numbers. PTA1–PTA5 are TMLE solutions using only PTA as starting point with different iteration numbers (100, 800, 2000, 3000, and 5000).

a certain value (>2000), the improvement was not significant. However, the computational burden was very high (see Fig. 8). For comparison, TMLE with more initial guess solutions but fewer iterations (300) showed a much better performance. It had a much lower RMSE and time cost. This implies that initial guess solutions play an instrumental role in TMLE. Increasing the source of the initial solutions is more significant than increasing the search time. Therefore, in the TMLE algorithm, we designed different regularization ways and used various regularization parameters to generate sufficient initial guess solutions.

D. Performance in Point Selection

After a consistent phase series estimation, the next critical step in DSI entails selecting a high-quality scatterer for further time-series processing. Posterior coherence is a widely used criterion for high-quality DS selections. First, we took the short-temporal coherence model as an example and compared the values of detR and posterior coherence in the TMLE and PTA methods. Previous studies have demonstrated that the cost function of the PTA algorithm can be transformed to a weighted interferometric phase fitness function [29]. Therefore, it is reasonable that the posterior coherence of PTA would be higher than TMLE [see Fig. 9(a)]. Conversely, when comparing the detR value between the TMLE and PTA algorithms, we discovered that TMLE had lower detR than PTA [see Fig. 9(b)]. Evidently, the TMLE solution is much less erroneous than PTA [see Fig. 9(c)], particularly for cases with small posterior coherence [see Fig. 9(d)]. It suggests that higher posterior coherence does not mean smaller RMSE. This finding implies that detR might be better than posterior coherence in describing the temporal coherence of a scatterer.

Furthermore, we explored whether detR can better distinguish scatterers with different coherences. Accordingly, we extended the short-term model (Coh1) to three models, by setting the parameter initial coherences (γ_0) to 0.6, 0.65, and 0.75, respectively. It was found that the slight variation in initial coherence (γ_0) did not inflict a significant difference for the distribution of posteriori coherence. Conversely, detR distributions using three input models are easily distinguishable (see Fig. 10), implying detR value can precisely distinguish scatterers with different statistical properties, and DS selection based on detR will be more accurate. Nevertheless, detR is not a normalized measurement. Its range of variance depends on SLC numbers. In the real case, we need to set a proper threshold according to specific situation.

V. Real-World Case Study

A. Study Area

We demonstrated the proposed method using a time-series of Sentinel-1 data over Shenzhen Airport, China (see Fig. 11). The test site included diverse land covers, such as buildings,

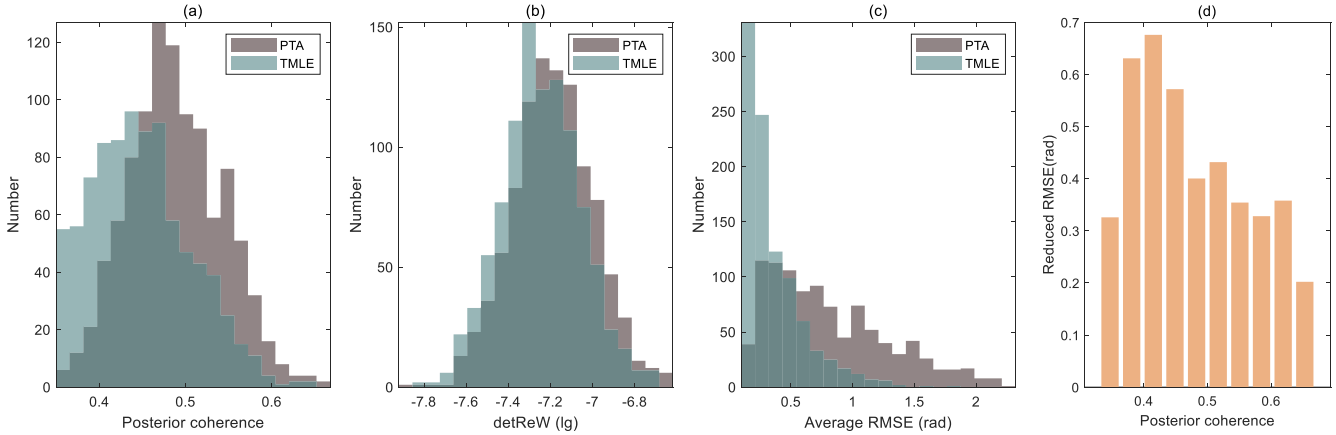

Fig. 9. (a)–(c) Histogram of posterior coherence, detR, and average RMSE from PTA and TMLE algorithms. (d) Reduced RMSE in the function of posterior coherence.

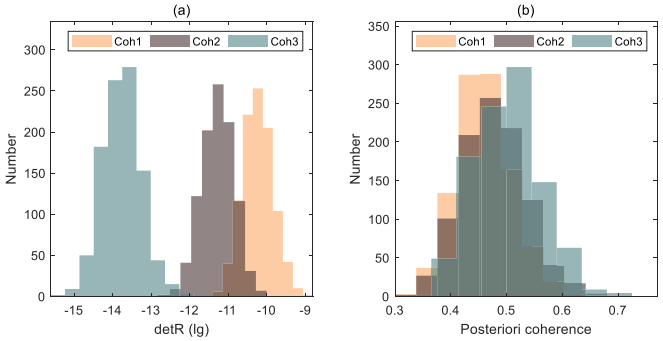

Fig. 10. (a) Histogram of detR using three different coherence models. (b) Histogram of posteriori coherence using three different coherence models.

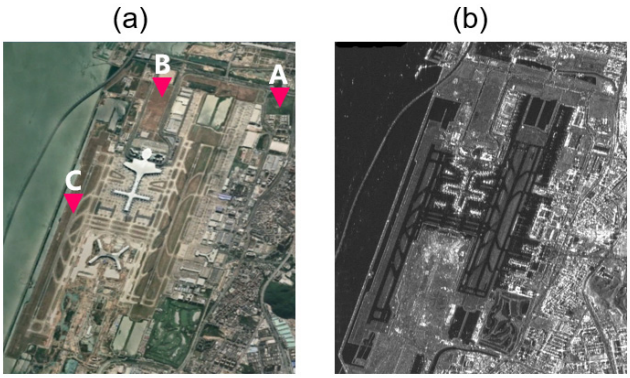

Fig. 11. Study area for the real-world case study in Shenzhen airport. (a) Optical image. (b) Averaged SAR intensity image. The red triangles correspond to the locations for three scatterers (A: grass, B: soil, and C: road) investigated in Fig. 13.

roads, soil, and grassland, providing opportunities to examine different scatterer types. Sentinel-1 images were captured in an ascending path using wide-swath mode. The observation period was from January 1, 2019, to March 20, 2020. During this period, 37 images were obtained with a revisit period of 12 days. The original SAR images were cut to 512 pixels $\times$ 1480 pixels size area. We adopted the Anderson–Darling test (p-value $= 0.05$) to select SHPs in a 7×15 patch. Only pixels with more than 50 SHPs were identified as candidate DSs. SAR observations of SHPs were considered as samples to calculate complex coherence matrices for each pixel. To better satisfy the stationarity assumption, the topographic component was removed from each SLC pair using a 12-m resolution TerraSAR tandem product. Because the pooled samples could not be simulated fairly, Reg 3 was not used in the simulation study. Here, we added it back to the case study to generate additional candidate solutions. For this regularization, we used a larger patch (21×45) to select more samples. The relatively large-size sample was used to calculate more stable pooled SCM, which was then taken to regularize the original SCM.

B. Validation of Phase Estimation

We started by validating the performance of phase estimation using the proposed likelihood function. The PTA algorithm, sharing the same single-scatter mechanism assumption, was used for comparison. However, it is impossible to obtain the true value in a real case. Therefore, two scenarios were designed for comparison. In Scenario one, we compared and investigated the difference between the retrieved consistent phase series from the two algorithms. In Scenario two, we implemented the validation using a parametric bootstrap approach. The first scenario revealed whether the difference caused by the proposed method was significant. The second scenario further validates whether the proposed method can perform well in a real coherence model.

To compare the differences, we used PTA and TMLE to separately retrieve consistent phase series (see Fig. 12). Both the PL approaches significantly improved the phase quality compared with the original single-look interferogram. However, visual inspection revealed that the difference between the phases retrieved using PTA and TMLE was not significant. This is because the study area comprises an urban area with many buildings and artificial infrastructure. There were a lot of PS pixels with SHP number less than 50. The phases were not re-estimated and were identical to the original single-look interferograms. No differences were expected. However, for DS-type pixels, the TMLE result was much less noisy than PTA, particularly in low-coherence areas, such as bare soil

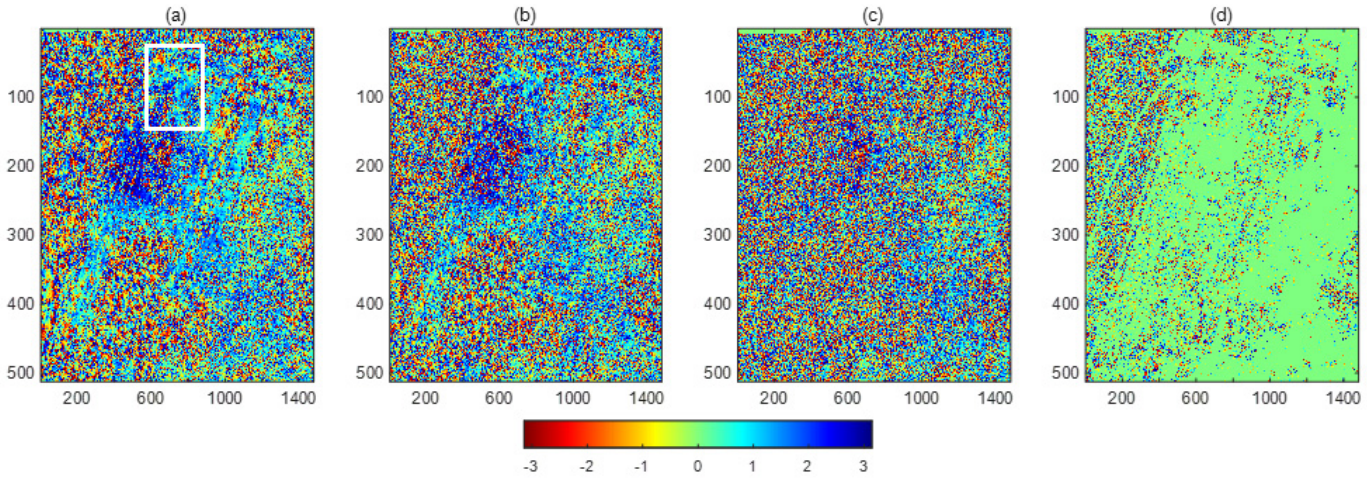

Fig. 12. Retrieved phase map on the last date. (a) TMLE. The white rectangle indicates the area to the enlarged in Fig. 9. (b) PTA. (c) Original single-look interferogram. (d) Phase difference between TMLE and PTA.

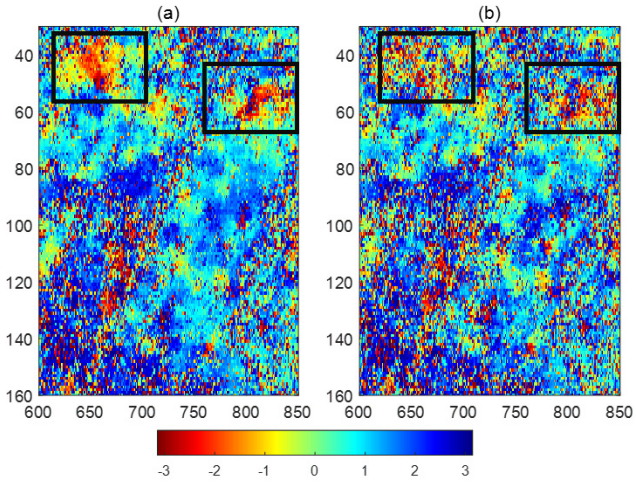

Fig. 13. Enlarged view of Fig. 7. (a) TMLE. (b) PTA. Black rectangles denote the areas with more obvious differences.

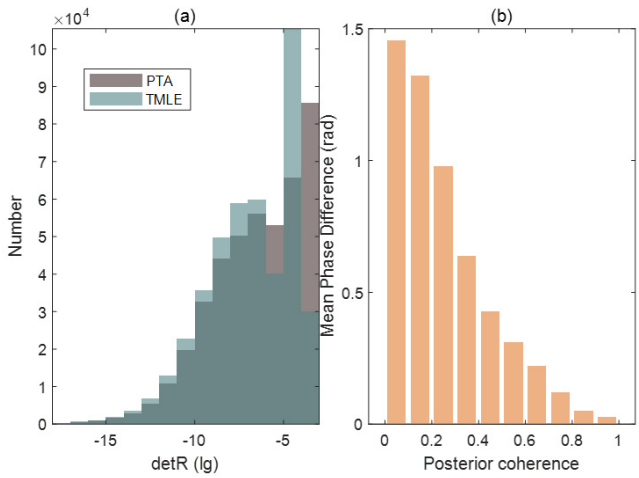

Fig. 14. (a) Histogram of detR from the PTA and TMLE algorithms. (b) Phase difference in the function of posterior coherence.

and grassland. In PTA, a slight regularization is allowed for the ill-posed SCM. In this case, regularization is gradually imposed and stops as long as the minimum eigenvalue is larger than a threshold value (0.1 in the present case). However, the proposed TMLE approach allows many attempts with different regularization approaches and regularization factors, providing opportunities for solutions using stronger regularization but with a greater likelihood.

Zooming in into the bare soil area with a significant difference, we found that the TMLE results were less noisy than PTA (e.g., the black rectangles in Fig. 13). For low-coherence pixels, SCM was poorly estimated and the likelihood function used in the PTA method was significantly biased. Therefore, PTA cannot provide a high-quality solution. Conversely, the TMLE approach relies on the true likelihood function. Although it is difficult to obtain the global maxima of likelihood, the traditional PL method using RSCMs with different regularization factors can assist in searching for a relatively optimal solution. It might not be the best method but should have a larger likelihood than PTA solution. Therefore, it is reasonable that TMLE provides smoother phase estimation with less noise.

Furthermore, we explored the histogram of detR results from two algorithms. The TMLE yielded smaller detR values than PTA. The result indicated that in the real case, the proposed method provides a solution with a larger likelihood. The difference in function of posterior coherence was plotted. Accordingly, the largest difference was distributed at the lowest posterior coherence and decreased gradually with the increase in posterior coherence (see Fig. 14). The result is consistent with the finding in our simulated experiments. It makes sense because the sampled complex coherence matrices have larger bias for low-coherent pixels. The PTA algorithm uses it to replace the real coherence matrix, and therefore bears more risks of contaminating the PL results. However, the proposed method can avoid this risk as it does not include such an approximation.

In the second scenario, parametric bootstrapping was applied to quantitatively compare the robustness of TMLE and PTA. Bootstrapping is a commonly used approach for

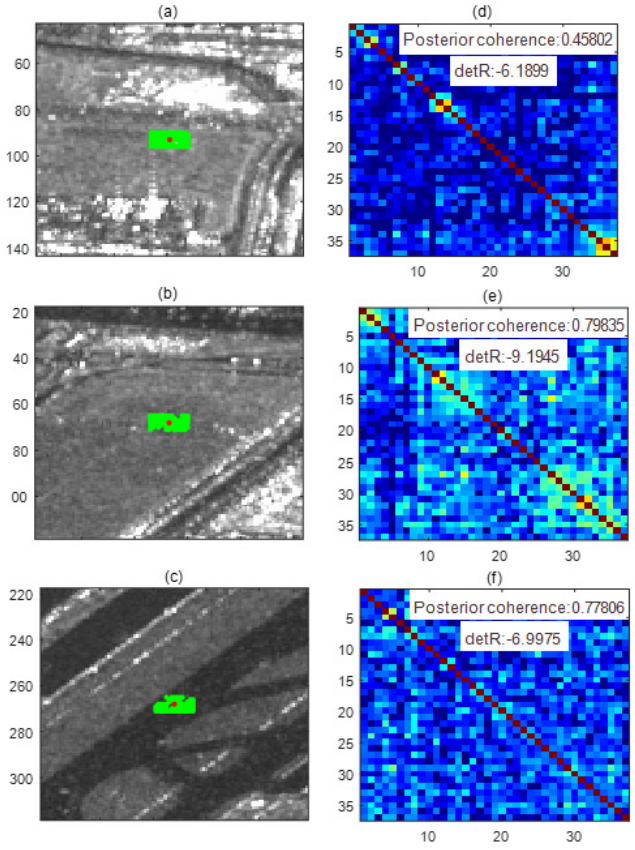

Fig. 15. SHP footprints and estimated coherence matrixes of three selected pixels in the study area. (a)–(c) Grass, soil, and road pixel footprints. (d)–(f) Grass, soil, and road pixel coherence matrixes.

evaluating estimator properties. We selected pixels from three typical land covers in the test area, that is, grass, soil, and roads [pixels A, B, and C in Fig. 9(a)]. The posterior coherences are 0.46, 0.80, and 0.78, respectively (see Fig. 15). A CGG distribution was assumed for time-series SAR observations. The parameters (i.e., coherence matrix and consistent phase series) were fitted using SAR observations. The fitted parameters were then considered as the ground truth and used to generate new random samples. The sample size was set to be the same as in the real case, that is, 93 for grass (pixel A), 84 for soil (pixel B), and 72 for road (pixel C).

As expected, the proposed TMLE algorithm had a lower RMSE than that of the PTA method for the three land types (see Fig. 16). According to our previous simulation, the proposed algorithm improved the results more significantly for low-coherence pixels. In this case, the selected road and grass pixels were less coherent than the soil pixels. Thus, we can observe more significant improvements in the grass and road pixels than in the soil. Maximum improvements of 0.43, 0.10, and 0.08 rad of RMSE were observed in the picked grass, road, and soil pixels, respectively. Compared with the simulation study as discussed in Section IV, TMLE exhibited a far greater improvement in the highly coherent pixels (soil and road) in the real case. This is because the sample size in the real case was relatively smaller than that used in the experiment. The SCM for highly coherent pixels is likely to be ill-posed, and regularization is required. The proposed TMLE approach searches for the optimal solution from a series of approximate MLE solutions using different regularization approaches and regularization factors. Therefore, it is expected to perform better than the conventional method with a single regularization parameter. Meanwhile, for the selected low-coherence glass pixel, the calculated coherence might be overestimated and has better coherence than the Coh 1 model in the simulation. Therefore, the improvement in TMLE is not as significant as that of the Coh 1 model in the simulation study. Overall, the parametric bootstrapping test indicates that the proposed TMLE is robust in a real-world case study. More specifically, it outperforms the conventional phase triangulation method for different complex coherence matrices and time-series phase patterns.

C. Validation of DS Selection

At present, posterior coherence is commonly used as an indicator to evaluate whether a consistent phase series is solved effectively and can provide support for high-quality DS point selection. Since detR directly reveals the likelihood of a solution, we believe it has the potential to act as an index for DS selection. As illustrated in Fig. 17, different land objects are more distinguishable in the detR map than posterior coherence. As depicted in Fig. 11(a), a large area in the upper left corner of the study area is covered by the ocean. It can be observed that water pixels have significantly smaller $-\lg(\text{detR})$ (i.e., smaller likelihood) than soil. Conversely, the posterior coherence of water pixels is indistinguishable from most soil scatterers.

Three typical pixels were selected to investigate the coherence matrices. Pixel 1 was a water scatterer with a low posterior coherence (0.25333). Pixels 2 and 3 were soil scatterers with low posterior coherence (0.23373) and high posterior coherence (0.72998), respectively (see Fig. 18). The coherence matrices indicate that Pixel 2 (soil scatterer) has a larger coherence than Pixel 1 (water scatterer) in most of the interferograms. This is reasonable, because a soil scatterer should be more stable than a water scatterer. The phase estimation likelihood ($-\text{detR}$) agrees with the expectation, where likelihood of Pixel 2 was significantly larger than Pixel 1. Conversely, the posterior coherence illustrates that Pixel 2 is less coherent than Pixel 1, failing to represent their true coherence in this case. Therefore, it is evident that the detR value can better describe the coherence of pixels than posterior coherence, agreeing with the findings given in the simulation study.

Furthermore, we selected detR as selection criterion to pick DS points. Accordingly, a threshold was set to ensure that water scatterers were not selected. For comparison purpose, we implemented PS-InSAR and conventional PTA DSI. DSs were jointly processed with PS points in the Stanford method for persistent scatterers (StaMPS) software. After re-estimating the temporal coherence in StaMPS, 31 313, 123 629, and 155 552 scatterers were left for PS-InSAR, conventional DSI, and the proposed approach, respectively. The deformation patterns shown in the velocity maps from the three processing frameworks mostly agree with each other. The primary

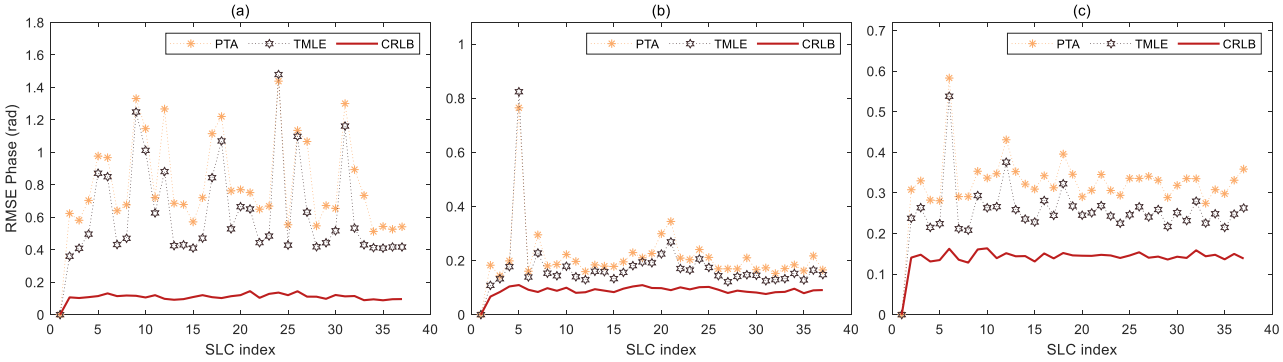

Fig. 16. RMSE comparison between PTA and TMLE. (a) Grass scatterer. (b) Soil scatterer. (c) Road scatterer.

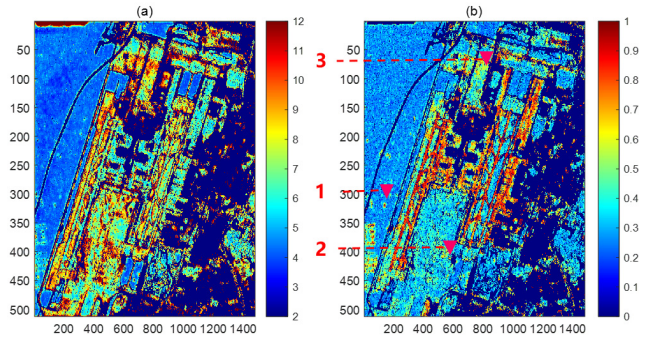

Fig. 17. Comparison of two DS selection criteria. (a) −lg(detR) map. (b) Posterior coherence map.

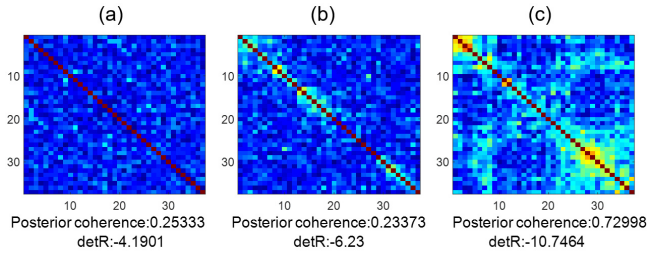

Fig. 18. Coherence matrixes for three typical scatterers. (a) Water. (b) Low-coherent soil. (c) High-coherent soil.

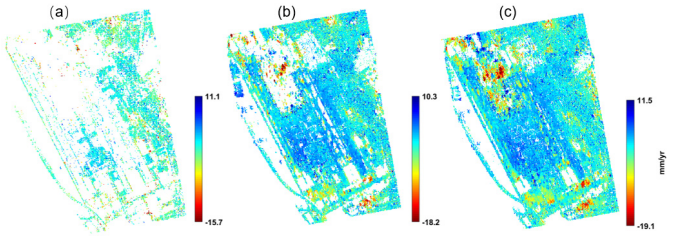

Fig. 19. Displacement rate maps. (a) PS-InSAR. (b) Conventional DSI. (c) Our proposed DSI.

difference originates from measurement density and coverage. The proposed approach further improved the density and coverage by integrating DSs and adopting the proposed detR function for phase estimation and DS selection (see Fig. 19). Due to increased density, more deformation details can be witnessed. Such improvement in the final deformation map benefits from two aspects by adopting the proposed framework: 1) TMLE gives more reliable consistent phase series results and 2) proper criterion based on detR function help pick high-quality pixels. The first reason guarantees that the estimated phase for DS has high quality, while the second reason ensures that these high-quality DSs will not be abandoned by improper selection criterion. Therefore, the combination of the two factors can ensemble more low-coherent pixels to the deformation map while retaining estimation quality.

VI. Conclusion

In this study, a new function (−detR) was proposed to evaluate the likelihood of consistent phase series. Unlike previous work, this function truly represents the likelihood without any assumption or approximation. Therefore, the proposed function can better describe the quality of a candidate solution. Based on this function, a DSI framework using this new function for phase optimization and DS selection was proposed. To mitigate the difficulty in searching global maxima of −detR, we adopted multiple starting points' strategy, which originates from phase triangulation solutions using a series of RSCMs with different regularization approaches and factors.

The simulation study reveals that the proposed phase estimation method (TMLE) outperforms the existing PL methods with significantly less RMSE, particularly for the low-coherence scenario, that is, short-term and periodic decorrelation models. Meanwhile, detR can better distinguish solutions from different coherence models than the widely used posterior coherence, exhibiting decent performance to serve as a quality measure for PL.

The real-world case study shows a finding similar to that of the simulation experiments. The difference between TMLE and PTA is distributed in a wide posterior coherence range, whereas it is more obvious for low-coherence pixels. TMLE provides a less noisy estimated interferogram than conventional PTA. The results from parametric bootstrapping show that TMLE has a lower RMSE than PTA for different types of scatterers. Furthermore, detR map also exhibits better performance than posterior coherence in distinguishing different scatterers. In particular, the water scatterer is more easily distinguished from the soil scatterer by detR than the posterior coherence. The final deformation map derived from the proposed DSI framework has significantly better DS density and coverage than the conventional approaches.

Future work needs to be done from two aspects: 1) further refining the solving algorithms in TMLE to reduce the

computational cost and make them efficiently converge to the global maxima and 2) extending the likelihood function from a single-scatter mechanism to multiple scatter mechanisms to enable the support of all types of scatterers in real-world applications.

REFERENCES

[1] C. Wang, X. Wang, W. Xiu, B. Zhang, G. Zhang, and P. Liu, "Characteristics of the seismogenic faults in the 2018 Lombok, Indonesia, earthquake sequence as revealed by inversion of InSAR measurements," *Seismolog. Res. Lett.*, vol. 91, no. 2A, pp. 733–744, Mar. 2020.

[2] C. Zhu, C. Wang, B. Zhang, X. Qin, and X. Shan, "Differential interferometric synthetic aperture radar data for more accurate earthquake catalogs," *Remote Sens. Environ.*, vol. 266, p. 112690, Dec. 2021.

[3] B. Osmanoğlu, F. Sunar, S. Wdowinski, and E. Cabral-Cano, "Time series analysis of InSAR data: Methods and trends," *J. Photogramm. Remote Sens.*, vol. 115, pp. 90–102, May 2016.

[4] D. H. T. Minh, R. Hanssen, and F. Rocca, "Radar interferometry: 20 years of development in time series techniques and future perspectives," *Remote Sens.*, vol. 12, no. 9, p. 1364, Apr. 2020.

[5] P. Berardino, G. Fornaro, R. Lanari, and E. Sansosti, "A new algorithm for surface deformation monitoring based on small baseline differential SAR interferograms," *IEEE Trans. Geosci. Remote Sens.*, vol. 40, no. 11, pp. 2375–2383, Nov. 2002.

[6] M. Manunta *et al.*, "The parallel SBAS approach for Sentinel-1 interferometric wide swath deformation time-series generation: Algorithm description and products quality assessment," *IEEE Trans. Geosci. Remote Sens.*, vol. 57, no. 9, pp. 6259–6281, Sep. 2019.

[7] A. Pepe, Y. Yang, M. Manzo, and R. Lanari, "Improved EMCF-SBAS processing chain based on advanced techniques for the noise-filtering and selection of small baseline multi-look DInSAR interferograms," *IEEE Trans. Geosci. Remote Sens.*, vol. 53, no. 8, pp. 4394–4417, Aug. 2015.

[8] A. Ferretti, C. Prati, and F. Rocca, "Permanent scatterers in SAR interferometry," *IEEE Trans. Geosci. Remote Sens.*, vol. 39, no. 1, pp. 8–20, Jan. 2001.

[9] M. Crosetto, O. Monserrat, M. Cuevas-González, N. Devanthéry, and B. Crippa, "Persistent scatterer interferometry: A review," *ISPRS J. Photogram. Remote Sens.*, vol. 115, pp. 78–89, May 2016.

[10] A. Hooper, D. Bekaert, K. Spaans, and M. Arikan, "Recent advances in SAR interferometry time series analysis for measuring crustal deformation," *Tectonophysics*, vols. 514–517, pp. 1–13, Jan. 2012.

[11] F. D. Zan and P. López-Dekker, "SAR image stacking for the exploitation of long-term coherent targets," *IEEE Geosci. Remote Sens. Lett.*, vol. 8, no. 3, pp. 502–506, May 2011.

[12] H. Ansari, F. D. Zan, and A. Parizzi, "Study of systematic bias in measuring surface deformation with SAR interferometry," *IEEE Trans. Geosci. Remote Sens.*, vol. 59, no. 2, pp. 1285–1301, Feb. 2021.

[13] S. Xiong, C. Wang, X. Qin, B. Zhang, and Q. Li, "Time-series analysis on persistent scatter-interferometric synthetic aperture radar (PS-InSAR) derived displacements of the Hong Kong–Zhuhai–Macao bridge (HZMB) from Sentinel-1A observations," *Remote Sens.*, vol. 13, no. 4, p. 546, Feb. 2021.

[14] Z. Sadeghi *et al.*, "Benchmarking and inter-comparison of Sentinel-1 InSAR velocities and time series," *Remote Sens. Environ.*, vol. 256, Apr. 2021, Art. no. 112306.

[15] F. Xue, X. Lv, F. Dou, and Y. Yun, "A review of time-series interferometric SAR techniques: A tutorial for surface deformation analysis," *IEEE Geosci. Remote Sens. Mag.*, vol. 8, no. 1, pp. 22–42, Mar. 2020.

[16] M. F. Fadhillah, A. R. Achmad, and C.-W. Lee, "Improved combined scatterers interferometry with optimized point scatterers (ICOPS) for interferometric synthetic aperture radar (InSAR) time-series analysis," *IEEE Trans. Geosci. Remote Sens.*, vol. 60, pp. 1–14, 2022.

[17] A. Ferretti, A. Fumagalli, F. Novali, C. Prati, F. Rocca, and A. Rucci, "A new algorithm for processing interferometric data-stacks: SqueeSAR," *IEEE Trans. Geosci. Remote Sens.*, vol. 49, no. 9, pp. 3460–3470, Sep. 2011.

[18] F. Rocca, "Modeling interferogram stacks," *IEEE Trans. Geosci. Remote Sens.*, vol. 45, no. 10, pp. 3289–3299, Oct. 2007.

[19] A. M. Guarnieri and S. Tebaldini, "On the exploitation of target statistics for SAR interferometry applications," *IEEE Trans. Geosci. Remote Sens.*, vol. 46, no. 11, pp. 3436–3443, Nov. 2008.

[20] B. Pinel-Puysségur, R. Michel, and J.-P. Avouac, "Multi-Link InSAR time series: Enhancement of a wrapped interferometric database," *IEEE J. Sel. Topics Appl. Earth Observ. Remote Sens.*, vol. 5, no. 3, pp. 784–794, Jun. 2012.

[21] S. Samiei-Esfahany, J. E. Martins, F. van Leijen, and R. F. Hanssen, "Phase estimation for distributed scatterers in InSAR stacks using integer least squares estimation," *IEEE Trans. Geosci. Remote Sens.*, vol. 54, no. 10, pp. 5671–5687, Oct. 2016.

[22] M. Jiang and A. Monti-Guarnieri, "Distributed scatterer interferometry with the refinement of spatiotemporal coherence," *IEEE Trans. Geosci. Remote Sens.*, vol. 58, no. 6, pp. 3977–3987, Jun. 2020.

[23] H. Song, B. Zhang, M. Wang, Y. Xiao, L. Zhang, and H. Zhong, "A fast phase optimization approach of distributed scatterer for multitemporal SAR data based on Gauss–Seidel method," *IEEE Geosci. Remote Sens. Lett.*, vol. 19, pp. 1–5, 2022.

[24] J. Bao *et al.*, "An improved distributed scatterers extraction algorithm for monitoring tattered ground surface subsidence with DSInSAR: A case study of loess landform in tongren county," *Int. J. Appl. Earth Observ. Geoinf.*, vol. 99, Jul. 2021, Art. no. 102322.

[25] A. B. Narayan, A. Tiwari, R. Dwivedi, and O. Dikshit, "A novel measure for categorization and optimal phase history retrieval of distributed scatterers for InSAR applications," *IEEE Trans. Geosci. Remote Sens.*, vol. 56, no. 10, pp. 5843–5849, Oct. 2018.

[26] Q. He, X. He, H. Zhuang, R. Wang, and J. Chen, "An improved method for phase triangulation algorithm based on the coherence matrix eigen-decomposition in time-series SAR interferometry," *IEEE Access*, vol. 9, pp. 150201–150212, 2021.

[27] Y. Wang and X. X. Zhu, "Robust estimators for multipass SAR interferometry," *IEEE Trans. Geosci. Remote Sens.*, vol. 54, no. 2, pp. 968–980, Feb. 2016.

[28] H. Ansari, F. D. Zan, and R. Bamler, "Sequential estimator: Toward efficient InSAR time series analysis," *IEEE Trans. Geosci. Remote Sens.*, vol. 55, no. 10, pp. 5637–5652, Oct. 2017.

[29] N. Cao, H. Lee, and H. C. Jung, "A phase-decomposition-based PSInSAR processing method," *IEEE Trans. Geosci. Remote Sens.*, vol. 54, no. 2, pp. 1074–1090, Feb. 2016.

[30] G. Fornaro, S. Verde, D. Reale, and A. Pauciullo, "CAESAR: An approach based on covariance matrix decomposition to improve multibaseline-multitemporal interferometric SAR processing," *IEEE Trans. Geosci. Remote Sens.*, vol. 53, no. 4, pp. 2050–2065, Apr. 2015.

[31] H. Ansari, F. De Zan, and R. Bamler, "Efficient phase estimation for interferogram stacks," *IEEE Trans. Geosci. Remote Sens.*, vol. 56, no. 7, pp. 4109–4125, Jul. 2018.

[32] A. Ferretti, A. Fumagalli, F. Novali, C. Prati, F. Rocca, and A. Rucci, "A new algorithm for processing interferometric data-stacks: SqueeSAR," *IEEE Trans. Geosci. Remote Sens.*, vol. 49, no. 9, pp. 3460–3470, Sep. 2011.

[33] M. Jiang and A. M. Guarnieri, "Distributed scatterer interferometry with the refinement of spatiotemporal coherence," *IEEE Trans. Geosci. Remote Sens.*, vol. 58, no. 6, pp. 3977–3987, Jun. 2020.

[34] S. Li, S. Zhang, T. Li, Y. Gao, Q. Chen, and X. Zhang, "An adaptive phase optimization algorithm for distributed scatterer phase history retrieval," *IEEE J. Sel. Topics Appl. Earth Observ. Remote Sens.*, vol. 14, pp. 3914–3926, 2021.

[35] C. Wang *et al.*, "Adaptive regularization of earthquake slip distribution inversion," *Tectonophysics*, vol. 675, pp. 181–195, Apr. 2016.

[36] N. Cao, H. Lee, and H. C. Jung, "Mathematical framework for phase-triangulation algorithms in distributed-scatterer interferometry," *IEEE Geosci. Remote Sens. Lett.*, vol. 12, no. 9, pp. 1838–1842, Sep. 2015.

Chisheng Wang received the B.S. degree from Beijing Normal University, Beijing, China, in 2007, the M.S. degree from the Institute of Applied Remote Sensing, Chinese Academy of Science, Beijing, in 2010, and the Ph.D. degree from the Department of Land Surveying and Geo-Informatics, The Hong Kong Polytechnic University, Hong Kong.

He is currently an Associate Professor with the School of Architecture and Urban Planning, Shenzhen University, Shenzhen, Guangdong, China. His research interests include developing algorithms for synthetic aperture radar (SAR) interferometry (InSAR) and light detection and ranging (LiDAR) data processing and applying them in infrastructure and disaster monitoring.

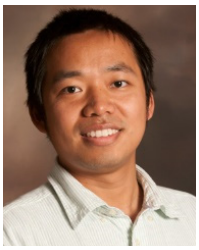

Xiang-Sheng Wang received the B.S. degree from the University of Science and Technology of China, Hefei, China, in 2004, and the Ph.D. degree from the City University of Hong Kong (jointly awarded by University of Science and Technology of China), Hong Kong, in 2009.

He is currently an Assistant Professor with the Department of Mathematics, University of Louisiana at Lafayette, Lafayette, LA, USA. His research interests include numerical optimization and approximation theory.

Yaping Xu received the Ph.D. degree in geography from Louisiana State University, Baton Rouge, LA, USA, in 2019.

He is currently with The University of Tennessee, Knoxville, TN, USA. He is leading the unmanned aerial vehicle (UAV) remote sensing project on biofuel crop monitoring that is collaborated with the Center for Bioenergy Innovation, Oak Ridge National Laboratory (ORNL), Oak Ridge, TN, USA, and funded by the Department of Energy (DOE), Washington, DC, USA. His research interests include integrating multi-scale remote sensing platforms with minimal field investigations to overcome geospatial scale challenges and limitations presented in smart agriculture, global and regional change, and human–environmental interactions.

Bochen Zhang (Member, IEEE) received the B.Eng. degree in geodesy and geomatics from the Nanjing University of Technology, Nanjing, China, in 2010, and the M.Sc. degree in geomatics and the Ph.D. degree in geodesy and geodynamics from The Hong Kong Polytechnic University, Hong Kong, in 2012 and 2020, respectively.

He is currently an Assistant Professor with the College of Civil and Transportation Engineering, Shenzhen University, Shenzhen, China. His research interests include developing techniques for space-borne and terrestrial radar interferometric data processing, with emphasis on geohazards and infrastructures' monitoring.

Mi Jiang (Senior Member, IEEE) received the B.S. degree in computational mathematics from the Nanjing University of Technology, Nanjing, China, in 2005, and the M.S. degree from Central South University, Changsha, China, in 2009. He is currently pursuing the Ph.D. degree with the Department of Land Surveying and Geo-Informatics, The Hong Kong Polytechnic University, Hong Kong, with emphasis on InSAR coherence estimation.

He started his studies on Synthetic Aperture Radar Interferometry (InSAR) with Central South University. He is currently an Associate Professor with Sun Yat-sen University, Guangzhou, China. During his Ph.D. research, he worked as a Guest Ph.D. Student at TU-Delft, The Netherlands, in 2013.

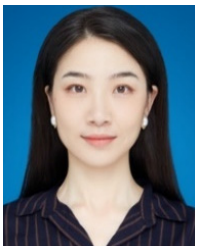

Siting Xiong received the B.Sc. degree from the School of Geodesy and Geomatics, Wuhan University, Wuhan, China, in 2011, the M.Sc. degree from the Department of Earth and Space Sciences, Peking University, Beijing, China, in 2014, and the Ph.D. degree from the Department of Space and Climate Physics, University College London, London, U.K., in 2019.

She was a Post-Doctoral Researcher with the College of Civil and Transportation Engineering, Shenzhen University, Shenzhen, China, during 2019–2021. She is currently an Associate Researcher with the Guangdong Laboratory of Artificial Intelligence and Digital Economy (SZ), Shenzhen. Her research interests include image processing, radar subsurface mapping, interferometric SAR, and planetary radar data processing.

Qin Zhang (Member, IEEE) received the Ph.D. degree in geodesy from Wuhan University, Wuhan, China, in 2002.

She is currently a Professor of geodesy and survey engineering with Chang'an University, Xi'an, China. She is currently working on high-precision geodetic data processing and algorithm development including global navigation satellite system (GNSS) and InSAR, and the monitoring and early forecast on geohazards, including land subsidence, ground fissures, and landslide.

Weidong Li received the M.S. degree in cartography and geographic Information engineering from the China University of Mining and Technology Beijing, Beijing, China, in 2005, and the Ph.D. degree in tectonic geology from the State Key Laboratory of Earthquake Dynamics, Institute of Geology, China Earthquake Administration, Beijing, in 2008.

Since 2012, he has been an Associate Professor with the Geographic Information System (GIS) Department, Henan University of Technology, Zhengzhou, China. His research interests include deep learning, geospatial analysis, and remote sensing information processing.

Qingquan Li received the Ph.D. degree in Geographic Information System (GIS) and photogrammetry from the Wuhan Technical University of Surveying and Mapping, Wuhan, China, in 1998.

From 1988 to 1996, he was an Assistant Professor with Wuhan University, Wuhan, where he became an Associate Professor, in 1996, and has been a Professor, since 1998. He is currently a Professor of Shenzhen University, Shenzhen, China; a Professor with the State Key Laboratory of Information Engineering in Surveying, Mapping and Remote Sensing, Wuhan University; and the Director of Shenzhen Key Laboratory of Spatial Smart Sensing and Service, Shenzhen. His research interests include intelligent transportation systems, 3-D and dynamic data modeling, and pattern recognition.

Dr. Li is an Academician of International Academy of Sciences for Europe and Asia (IASEA), an Expert in Modern Traffic with the National 863 Plan, and an Editorial Board Member of the *Surveying and Mapping Journal* and the Wuhan University Journal—*Information Science Edition*.